



## OPEN Pop the bubbles and let the current flow: mechanochemistry of micron and nano-sized openings in dielectric layers

Gizem Birant<sup>1,2,3</sup>✉, Christian Rossi<sup>4</sup>, Jan Czech<sup>1,2</sup>, Wouter Marchal<sup>1,2</sup>, Guy Brammertz<sup>1,2,3</sup>, Tom Aernouts<sup>1,2,3</sup>, Diego Colombara<sup>4</sup>, Jessica de Wild<sup>1,2,3</sup> & Bart Vermang<sup>1,2,3</sup>

Thin or ultra-thin dielectric layers have been widely used in various applications such as capacitors, piezo-electrics, and solar cells. This study explains the mechanism and chemistry of creating nano- and micron-sized openings in atomic-layer-deposited aluminum oxide-based dielectric layers using the alkali metal salt selenization technique. The necessary components for this mechanism are excess methyl groups present in the dielectric layer, supply of selenium and alkali metals, and a minimum annealing temperature. It is shown and explained that to create openings in the dielectric layer, heavier alkali halide metal salts require less energy, or - in other words - a lower annealing temperature. The overall hypothesis is explained via a thermodynamic approach with supportive thermochemical reactions. Thus, an easy way to engineer the dielectric layer to form openings at low temperatures is presented, beneficial for various applications like photovoltaics, optoelectronics, or micro-electro-mechanical systems (MEMS).

**Keywords** Enthalpy of the alkali-halide metal salts, Thermochemistry, Aluminum oxide based dielectric layer, TD-GC-MS measurement, Dimethyldiselenide

Nowadays, aluminum oxide ( $\text{AlO}_x$ ) is one of the most preferred dielectric layers for optoelectronic applications<sup>1</sup>, micro-electro-mechanical systems (MEMS)<sup>2</sup>, or various other applications in the semiconductor industry<sup>3</sup>. Another prominent usage area of  $\text{AlO}_x$  is the solar cell industry, in which it is applied to passivate the rear or front interface of thin film-based solar cells<sup>4-7</sup>. There are various ways to apply this passivation layer. One of the most preferred is atomic layer deposition (ALD) because its working principle is relatively simple, and it offers homogeneously deposited layers. It is based on gaseous chemical precursors that react with the surface with sequential varying pulses; a detailed explanation of the process is described in<sup>8</sup>.

The significant passivation properties of the  $\text{AlO}_x$  layer for the rear surfaces of solar cells have been proved by many research groups, see<sup>9-11</sup>. One challenge when applying a dielectric layer is to ensure the current flow, i.e., to avoid blocking the flow. This is achieved by making the layer sufficiently thin, so tunnelling is possible, or by making contact openings in the dielectric layer. To create these openings, lithography techniques, either nanoimprint or e-beam, are commonly used<sup>12,13</sup>. However, lithography is an expensive and time-consuming tool to reach this aim. Hence, industrially viable approaches have been sought and found in recent years<sup>14,15</sup>. Selenization of prepared  $\text{AlO}_x$  layer in presence of alkali metals is one of these approaches. It is based on spin-coating or evaporation<sup>16</sup> the alkali halide metal salt solution on the dielectric layer, followed by exposure to selenium. In the case of CIGS solar cells, the openings emerge naturally during the absorber layer deposition<sup>9</sup> or selenization prior to absorber layer deposition<sup>17</sup>.

In this present contribution, the mechanism and chemistry behind the formation of these openings are studied in detail. A model based on the chemical potential of the various alkali metal compounds and elemental gaseous selenium is presented and experimentally verified by applying different temperatures, annealing times, and alkali salts to make the contact openings in the  $\text{AlO}_x$  layer. With thermal desorption gas chromatography-mass spectrometry measurements (TD-GC-MS), the formation of dimethyl diselenide ( $\text{DMDSe}$ ,  $\text{C}_2\text{H}_6\text{Se}_2$ ) was verified, and correlated to the formation of the openings in the passivation layer.

<sup>1</sup>Hasselt University, imo-imomec, Martelarenlaan 42, 3500 Hasselt, Belgium. <sup>2</sup>imec, imo-imomec, Thor Park, 8320 Genk, Belgium. <sup>3</sup>EnergyVille, imo-imomec, Thor Park 8320, 3600 Genk, Belgium. <sup>4</sup>Department of Chemistry and Industrial Chemistry, University of Genova, via Dodecaneso 31, Genova 16146, Italy. ✉email: birantgizem@gmail.com; gizem.birant@imec.be

## Experimental details and characterization methods

### Sample preparation

The samples are always made on the same substrate, i.e., soda-lime glass (SLG) with Si (O, N) barrier and 300 nm thick Molybdenum (Mo) layer. The Si(O, N) suffice as alkali barrier and no alkali is coming from the glass. Dielectric layers, 4 nm and 6 nm, are deposited via ALD at 300 °C by using tri-methyl aluminum (TMA) as the precursor and H<sub>2</sub>O as the reactant. By Woollam RC2 spectroscopic ellipsometer, the deposition rate was extracted to be 0.17 nm/cycle (previously measured for growth on silicon wafers), and the growth rate is assumed to be constant. The alkali halide metal salt solutions are prepared by mixing the pure alkali salt powder with de-ionized water and spin-coated on the dielectric layers at 3000 rpm until all the water on the surface is gone, and only the salt crystals are left: ~10 s. The selenization is realized in a quartz furnace at various temperatures (200 °C to 540 °C), and pure selenium pellets are used as the selenium source. (Fig. 1)

The layer sequence of the final structure is the following for all the samples with alkali barrier, except the ones for TD-GC-MS: SLG/Si(O, N)/Mo/AlO<sub>x</sub>/Alkali salt. For the samples without alkali barrier, no salt is deposited. For the TD-GC-MS measurement, the selenium is deposited in the same quartz furnace prior to AlO<sub>x</sub> layer, and the sequence is the following: SLG/ Si(O, N) (barrier layer)/Mo/Se/AlO<sub>x</sub>/Alkali halide metal salt. For TD-GC-MS measurement, one more type of structure is used. This time the substrate is altered to SLG without the barrier to test the sodium ion coming from the glass instead of depositing the halide alkali salt.

### Characterization methods

The existence, size, shape, and population of the openings are detected by scanning electron microscopy (SEM) imaging and energy-dispersive X-ray spectroscopy (EDS) analysis with a Tescan and Bruker SEM with secondary electron detector. The acceleration voltage is different from sample to sample and ranging between 10 kV and 15 kV. The outgassing during the selenization is detected via thermal desorption gas chromatography mass spectrometry (TD-GC-MS). For this measurement, the prepared samples are crushed into small pieces to fit into the thermal desorption tubes. The tubes are loaded in a Markes TD-100 thermal desorption. Then, the tool is heated up to 250 °C under a continuous He flow and held for an isothermal period of 10 min. The evolved gases are transferred to a GC setup (Thermo<sup>®</sup> trace ultra, Agilent DB5-MS column) coupled to an ISQ7000 quadruple MS detector. Components are identified by the NIST-MS library and selenium-containing compounds were attributed with MF and RMF factors > 850. Both total ion current (TIC) and ion-selective chromatograms were extracted.

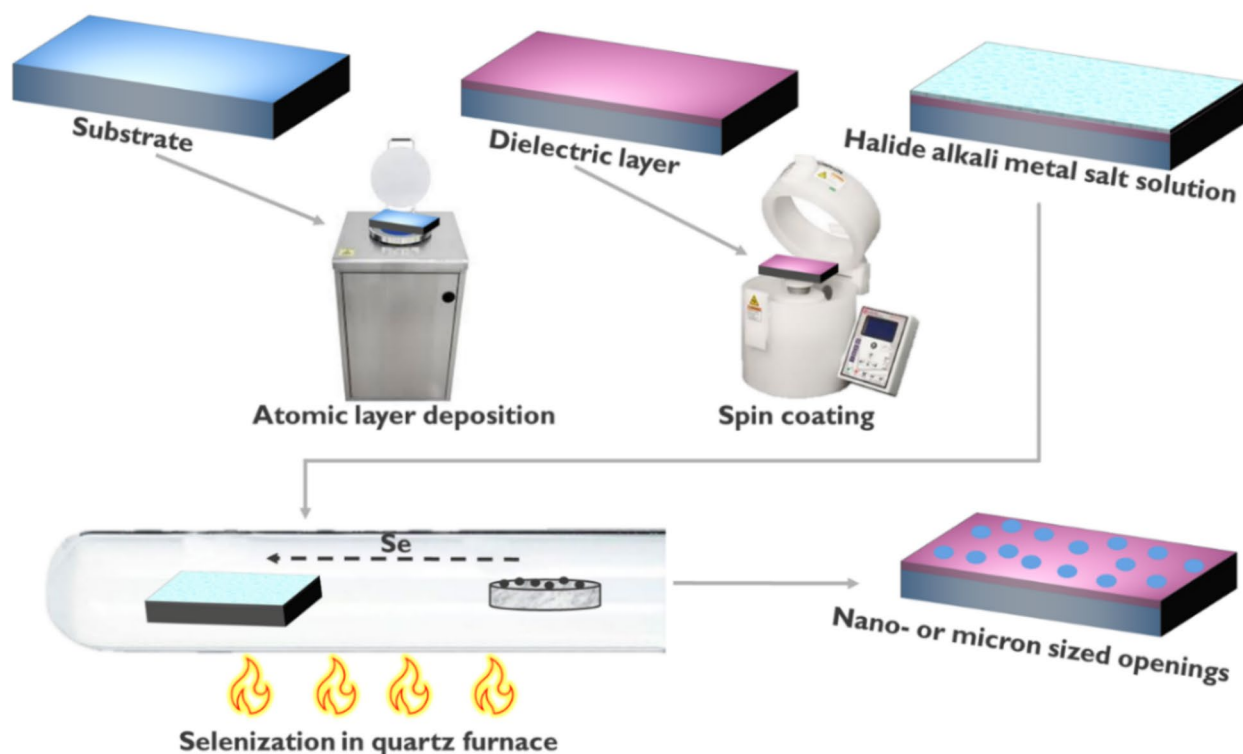


**Fig. 1.** Sample preparation sketch. The dielectric layers are deposited by ALD. Then, the alkali halide salt solution is spin coated on the dielectric layer. Afterwards, the sample is selenized in a quartz furnace to create the openings in the dielectric layer.

## Results and discussion

### Creation of the openings

In this study, the alkali halide salt selenization technique is used to create the openings in the  $\text{AlO}_x$  dielectric layer. In our previous study, we showed that during the CIGS deposition, contact openings can be realized in the  $\text{AlO}_x$  dielectric layer during the absorber layer deposition process<sup>9</sup>. There are three features in this process that play a crucial role: selenium (at a certain temperature), alkali salt solution (at a certain concentration), and trapped (methyl-containing) gases inside the non-stoichiometric ALD  $\text{AlO}_x$  layer which contains precursor traces. The details of the nature of the trapped gases can be found elsewhere<sup>18</sup>. In order to test the role of these three features, four experimental sets are prepared. The schematic representations of the experiments are shared in Fig. 2, while the SEM images of realized experiments are shared in Fig. 3.

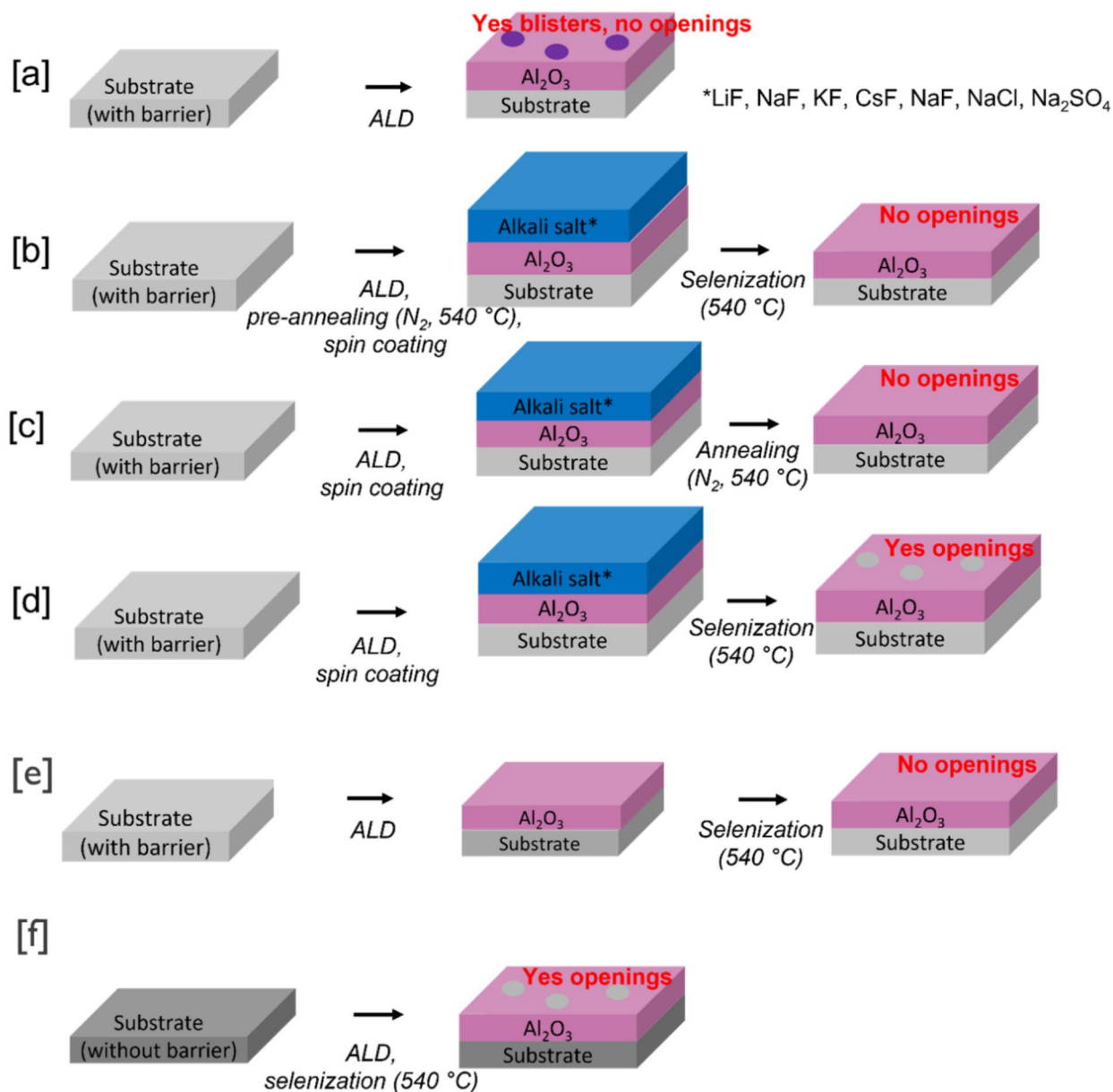
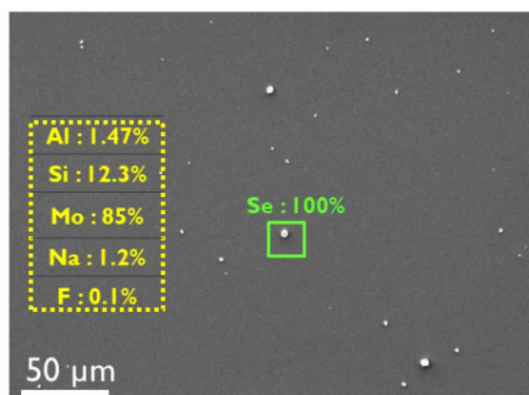
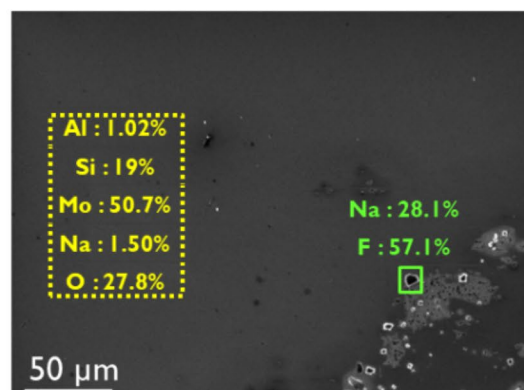


**Fig. 2.** Schematic depiction of the experimental evidence. (a) ALD deposition onto an SLG substrate with barrier showing the formation of blisters in the dielectric layer. (b) ALD deposition onto an SLG substrate with barrier followed by a pre-annealing step to release the blisters in the layer; afterward, alkali salt is spin-coated, and then the substrate is selenized (no openings formation). ALD deposition onto an SLG with barrier followed by spin coating of alkali solution annealed in (c)  $\text{N}_2$  atmosphere at  $540^\circ\text{C}$  (no openings formation) or (d) selenized at  $540^\circ\text{C}$  (openings are formed). (e) ALD deposited alumina layer onto SLG with barrier without alkali salt deposition step is selenized at  $540^\circ\text{C}$  (no openings formation). (f) ALD deposited alumina layer onto SLG without any barrier was selenized at  $540^\circ\text{C}$  (openings are formed).

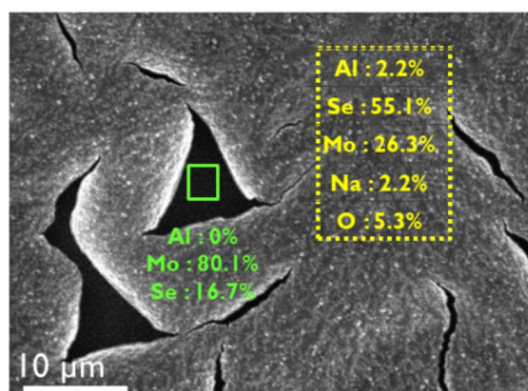
[a]  $\text{AlO}_x$  without openings  
**Annealed prior** to standard selenization  
 NaF salt solution



[b]  $\text{AlO}_x$  without openings  
 **$\text{N}_2$  Annealing**  
 NaF salt solution



[c]  $\text{AlO}_x$  with openings  
**Standard selenization**  
 NaF salt solution



[d]  $\text{AlO}_x$  without openings  
 Standard selenization  
**without NaF salt solution**

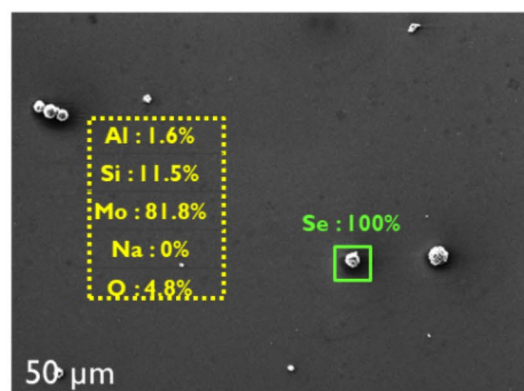


**Fig. 3.** Top view SEM images of four samples, all of which have a 6 nm thick  $\text{AlO}_x$  layer. (a) Sample with 0.4 M NaF, and pre-annealed to remove methyl residues from within the  $\text{AlO}_x$  layer. (b) Sample with 0.4 M NaF salt solution, which underwent annealing under nitrogen, i.e., without selenium. (c) Sample with 0.4 M NaF salt solution, which underwent standard selenization process, i.e., selenized under 540 °C for 10 min. (d) Sample without the alkali salt solution, which underwent standard selenization. *Openings are detected only in the samples where all three features in the equation are present: selenium, NaF and methyl residues.*

Here following several key experiments will be described with the aim of understanding the reaction mechanism responsible for the holes' formation. Unless specified differently, all the substrates are SLG with a barrier to prevent the diffusion of  $\text{Na}^+$  into the material. When an alumina layer is grown onto the substrate, some blisters are observed but no openings are formed (Fig. 2a and S1). When the same ALD deposition is followed by a pre-annealing at 540 °C in a nitrogen atmosphere to release the blisters, an alkali treatment and a selenization at 540 °C again no openings are formed (Fig. 2b). As shown by Fig. 3-a, the openings creation is obstructed if the  $\text{AlO}_x$  layer is pre-annealed. The particles on the surface are pure selenium particles, verified with the EDS.

Similarly, when no pre-annealing is involved, alkali is deposited through spin-coating and the selenization of the previous attempt is replaced by an annealing in  $\text{N}_2$  atmosphere at 540 °C, no openings are observed (Fig. 2c). The SEM image shows no openings in the dielectric layer (Fig. 3-b). The EDS measurement, on the other hand, reveals that the NaF salt particles remain on the surface with the absence of selenium in the environment. While, if both alkali treatment and selenization are involved without any pre-annealing holes are successfully formed in

the alumina layer (Fig. 2d). As can be seen from the SEM picture in Fig. 3-c, openings are created in the dielectric layer. To prove the existence of the openings, EDS measurement shows aluminum at 2.2 wt% on the layer and 0 wt% on the dark part, i.e., the opening (inset). On the other hand, if alkali salt selenization step is removed, and only the ALD deposited dielectric layer is selenized, no openings are formed (Fig. 2e). In the absence of the alkali salt solution, the creation of the openings is inhibited. It is obvious from the SEM picture shared in Fig. 3-d, there are no openings detected in the  $\text{AlO}_x$  layer. The particles on the surface are identified as pure selenium particles by EDS. Lastly, when a substrate without any barrier is involved and no alkali is deposited, after the selenization process the openings are distinguished (Fig. 2f). The as discussed experimental evidence suggest the need for blisters in the dielectric layer, selenium and alkali in order to have the formation of the holes.

### Which ion is needed, the cation ( $\text{Na}^+$ ) or the anion ( $\text{F}^-$ )?

After identifying the key features for the openings' creation, we make the elemental analysis to obtain more detailed insights into the morphological changes of the surface. We started this analysis with the NaF salt solution. The aim is to check whether the cation,  $\text{Na}^+$ , or the anion,  $\text{F}^-$ , is helping the process. To this end, we exchanged the fluoride ions with sulfate ( $\text{SO}_4^{2-}$ ) and chloride ( $\text{Cl}^-$ ) species and used a 6 nm thick  $\text{AlO}_x$  dielectric layer. We also considered the sodium ion coming from the glass by changing our substrate from SLG with barrier to SLG without the barrier. For this experiment, we used a 4 nm thick  $\text{AlO}_x$  dielectric layer, because this approach is not suitable for thicker  $\text{AlO}_x$  layers, kindly refer to Figure S2 for details. As shown in Fig. 4, openings are created for all samples, implying that the cation part is the key reactive component of the process. Even for  $\text{Na}^+$  ions coming from the glass, i.e., no mobile counter ion is involved in the process, openings are detected in the dielectric layer.

### Is it possible to use other alkali halide metal salts?

Until so far, we have investigated the openings that are created by sodium-based salt solutions. However, it is possible to create the openings with potassium fluoride salt solution as well<sup>15</sup>. This means that other alkali halide metal salts can also be used for this approach.

Considering we applied heat treatment, i.e., selenization, to our substrates, we examined the lattice dissociation enthalpies ( $U_0$ ) and size of the unit cells of these salts. The size of the unit cells increases step by step from LiF to CsF through the first group of the periodic Table<sup>6</sup>. On the contrary, the  $U_0$  and thermal stability decrease from LiF to CsF, (Fig. 5)<sup>6</sup>. This information suggests that lower selenization temperatures for heavier alkali halide metals may be possible.

A systematic temperature variation study was conducted to establish the correlation between the different alkali fluoride salt treatments and the required temperature for opening formation. For this purpose, the alkali fluoride salts were spin-coated on substrates with a 6 nm thick  $\text{AlO}_x$  dielectric layer. Since we are using Se pellets for selenization, the starting temperature of the test was chosen as 200 °C, i.e., the melting point of Se<sup>19</sup>.

As observed in Fig. 6, the upper SEM images show the as-deposited version of the salt solutions (Fig. 6a to d), while the bottom ones show the created openings after selenization at various temperatures (Fig. 6e to h).

At 200 °C, we only observed openings for 0.1 M CsF salt solution. The Y-shaped opening results from the shape of the salt crystals, i.e., CsF salt particles accumulated as a Y-shape, see Fig. 6a vs. e. This implies that the openings are created at the exact locations where the salts are deposited. Hence, controlling the salt deposition enables to engineer the distribution of openings. Then we increase the temperature step by step to determine the minimum temperature required for each individual alkali to induce the opening within the set timeframe. We call this temperature the *threshold* temperature. As shown by Fig. 6, the threshold temperature for RbF is 250 °C, while it is 350 °C for KF and 540 °C for LiF. Since the duration of the CIGS deposition is approximately 10 min, we always use the same dwell time in the annealing process. However, for LiF, 10 min was not enough to create the openings; in this case, we managed to achieve nano-sized openings after doubling the dwell time (Fig. 6h).

The results of the image analysis and the observed trends in threshold temperatures are summarized in Fig. 7, along with each alkali fluoride's lattice enthalpy.

As shown in the graph, the threshold temperature and lattice enthalpy exhibit a strong positive linear relationship, with a calculated Pearson correlation coefficient of 0.989. This high value indicates a nearly perfect correlation between the two variables, confirming a significant and consistent linear association. The smaller the required energy per mol to dissociate the salt, i.e., the lattice enthalpy ( $U_0$ ), the lower the threshold temperature. For instance,  $U_0$  for LiF is 1034 kJ/mol, and the required temperature is 540 °C, while it is 200 °C for CsF with 744 kJ/mol lattice enthalpy. Another comparison can be made between NaF and LiF. Although the observed threshold temperature is the same, the time needed to create the openings with LiF is twice compared to NaF,

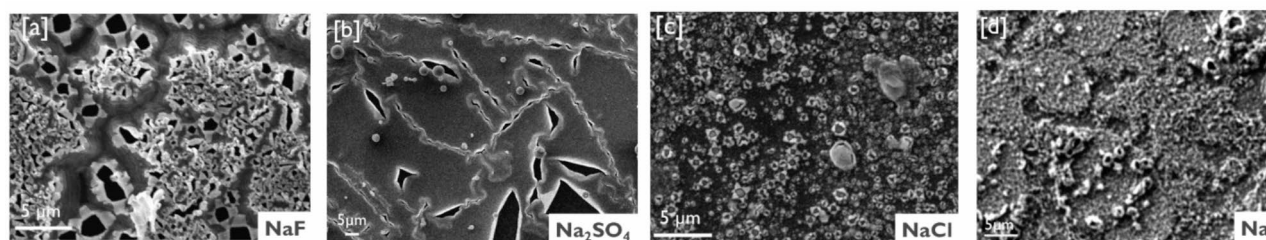


**Fig. 4.** Openings are created by using (a) NaF, (b)  $\text{Na}_2\text{SO}_4$ , and (c) NaCl salt solutions. (d) For Na ions coming from the glass, openings are also visible in the dielectric layer.

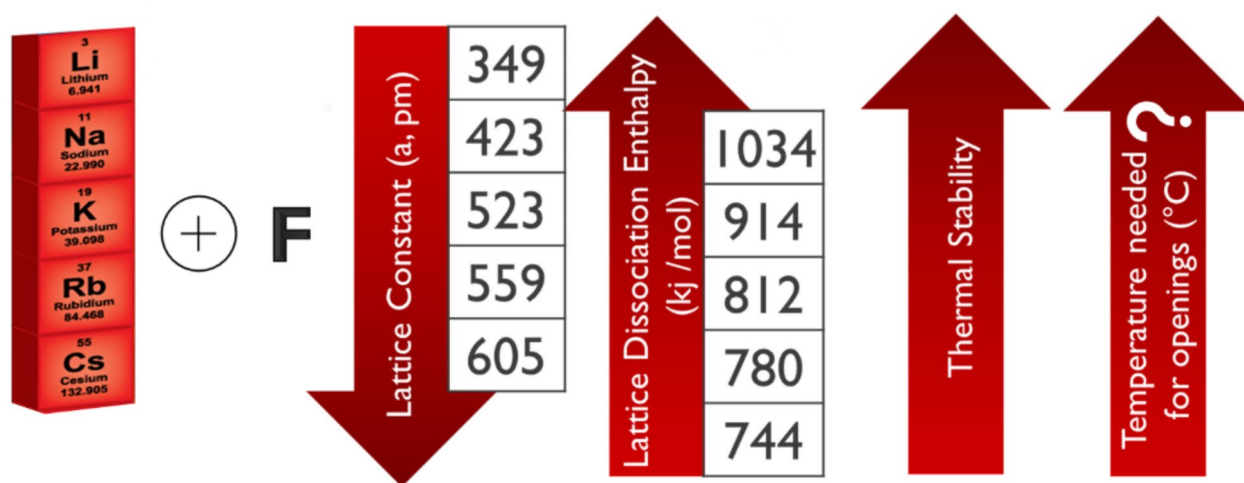


**Fig. 5.** Periodic table trends of lattice constants and lattice dissociation enthalpies for alkali fluorides, pointing to decreasing thermal stability along the group. *These trends coincide qualitatively with the corresponding empirical trend of decreasing temperature identified as needed to induce the openings.*

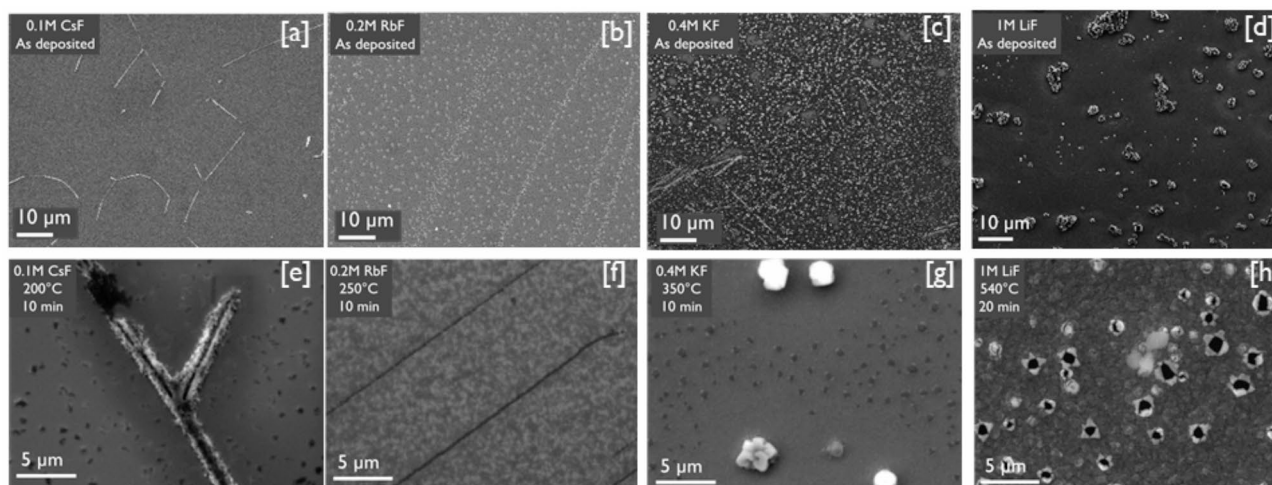


**Fig. 6.** Top-view SEM images of the substrates with as-deposited alkali halides (a–d), and corresponding openings in the  $\text{AlO}_x$  layer induced after selenization at 200 °C for CsF, 250 °C for RbF, 350 °C for KF and 540 °C for LiF (e–h). *Images are not correlative.*

due to the difference in their lattice enthalpies. Thermodynamic properties and reactivity of substances are often correlated, as historically reported by Hammett<sup>20</sup> for organic compounds, and later extended by Sverjensky and Molling<sup>21</sup> to inorganic crystals, and Colombara<sup>22</sup> to reactive annealing of thin films. Hence, the empirical relationship in Fig. 7 provides sound evidence that the formation of openings is driven by a chemical reaction involving the alkali salts. It is important to emphasize that lower temperatures may be required to induce the openings, depending on the nature of the alkali source. For example, sodium ions released by the glass substrate can also create openings, but can do so even at 250 °C, i.e., at much lower temperature than the 540 °C needed when using the NaF salt solution. Details of the mechanism are discussed in the following section.

### The mechanism and the chemistry behind this process

In this work, holes are spontaneously formed in a thin alumina ( $\text{AlO}_x$ ) layer prepared through ALD in the presence of alkali ions and after a selenization process. Interestingly, such openings present a peculiar shape with removed alumina pieces oriented to the outer of the hole resembling the remnants of micro-explosions (Figure S3). As shown in Fig. 8, TD-GC-MS revealed the formation of gaseous dimethyl diselenide ( $\text{CH}_3\text{SeSeCH}_3$ ) and some carbon selenide ( $\text{CSe}_2$ ), which suggests that the holes may indeed result from the buildup of an inner overpressure.

The mechanism of this process has been explained in detail in "Results and discussion", Fig. 2. In this section, the mechanochemistry of this process will be defined with the help of two different models.

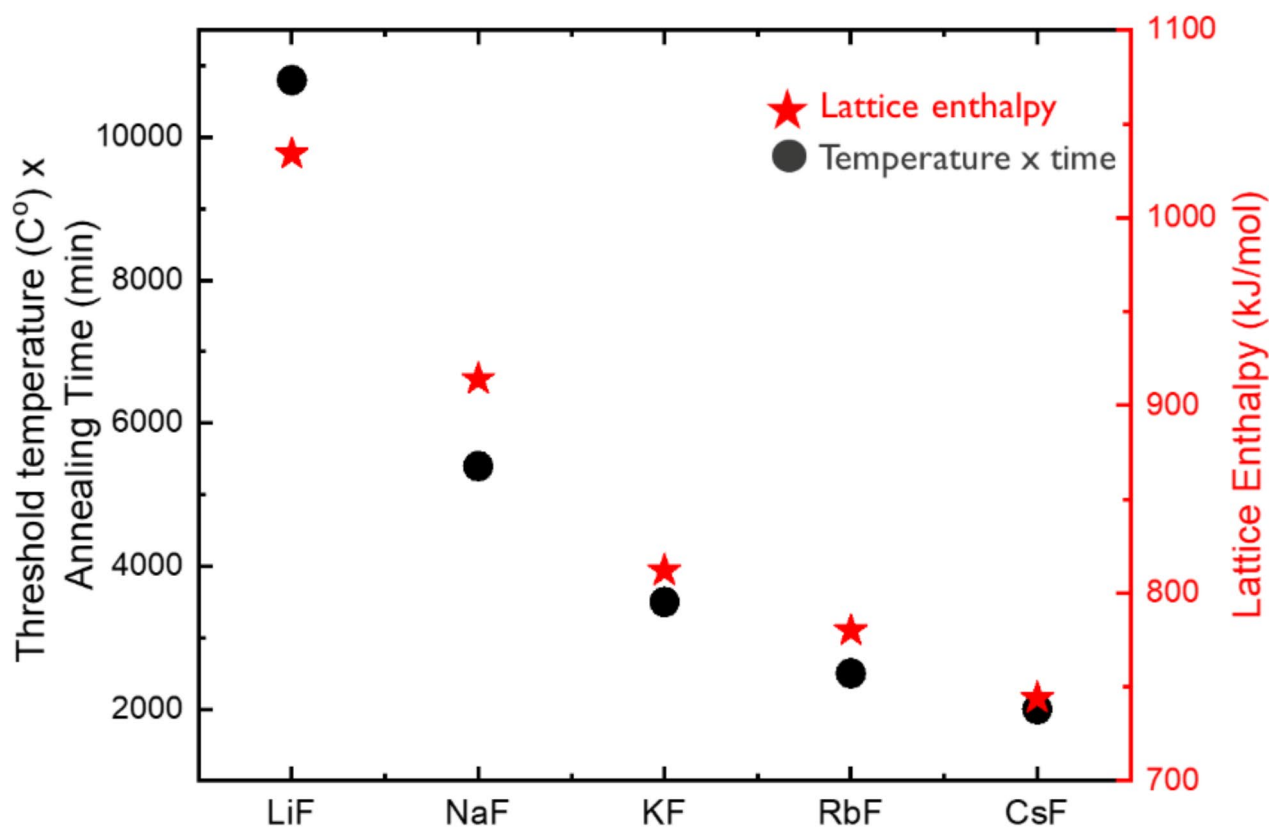


**Fig. 7.** Correlation between the temperature needed to create the openings (threshold temperature) multiply with the needed annealing time and the lattice enthalpies of the alkali fluorides. Data supporting Fig. 7 is available as supporting excel file named “Threshold temperature vs. enthalpy data”.

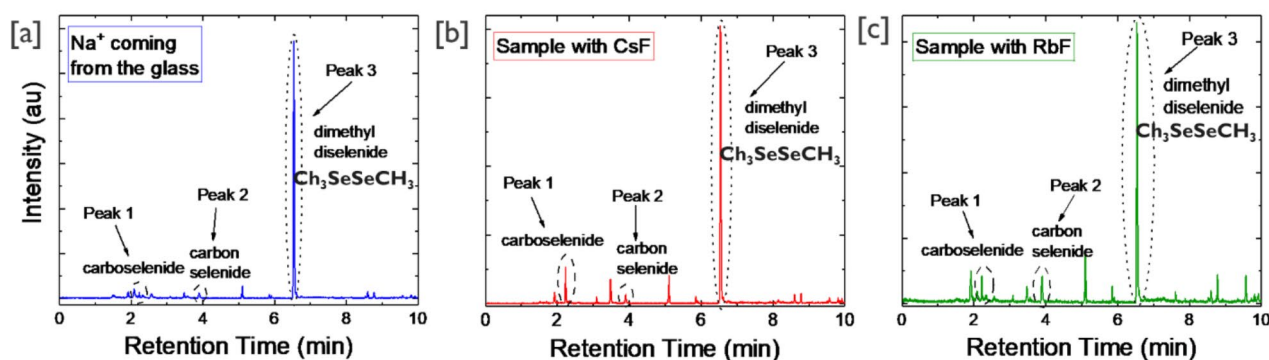
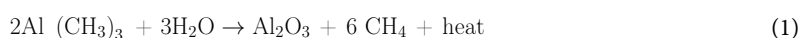


**Fig. 8.** TD-GC-MS analysis. Three  $\text{AlO}_x$  samples were prepared through ALD in the presence of (a)  $\text{Na}^+$  coming from the substrate, (b) CsF and (c) RbF. The last two were spin-coated onto the alumina surface, and all three samples were followed by selenization at  $250^\circ\text{C}$  in an inert atmosphere. (Selenium is supplied from the prior deposition.) Data supporting Fig. 8 is available as supporting excel file named “TD-GC-MS data”.

### Model part 1: the initial idea

During ALD, trimethyl aluminum anchoring steps are followed by water vapor cycles, yielding an  $\text{AlO}_x$  layer according to reaction 1. By modifying the number of steps, the total thickness of the alumina layer can be controlled<sup>23</sup>.



However, as shown with FTIR analysis by Dillon et al.<sup>24</sup>, some unreacted methyl groups might remain even after the water converts the trimethyl aluminum into alumina. This view is supported in our case by the observation of enhanced wettability of the alumina by water after ozone treatment. Ozone is often exploited in place of H<sub>2</sub>O to react with Al(CH<sub>3</sub>)<sub>3</sub> and produce Al<sub>2</sub>O<sub>3</sub>. As reported by Goldstein et al.<sup>25</sup> the -CH<sub>3</sub> can react with O<sub>3</sub> following two different reaction pathways. Oxygen may enter inside the C-H bond forming a hydroxyl group (i) or inside the Al-C bond producing a methoxy group (ii). Both reaction mechanisms (i, ii) end up forming Al<sub>2</sub>O<sub>3</sub>. The wettability change suggests that a surface reaction is ongoing, and it can be justified only by the presence of -CH<sub>3</sub> terminated surface, (Fig. 9a). Pre-annealing in nitrogen does not show the formation of any openings, as it is known that higher annealing temperatures remove -OH and -CH<sub>3</sub> groups more effectively<sup>24</sup>. Lastly, at the end of the ALD deposition, several blisters of various sizes of about a few tens of microns are observed (Figure S1). Since only two gaseous species are water and trimethyl aluminum, it is likely that the gas trapped inside the blisters is trimethyl aluminum. Consequently, the unreacted CH<sub>3</sub> might also come from such blisters.

These facts provide indirect evidence that unreacted methyl groups on the alumina surface are linked to the release of dimethyl diselenide following a reaction with selenium upon exposure to the alkali solution and elemental selenium. Dimethyl diselenide has a boiling point of about 155–157 °C, hence it is present as a gas in the reaction environment (540 °C) (Fig. 9b). It is hypothesized that such a gas generates an overpressure inside the material which breaks the alumina layer (Fig. 9c). It is worth noting that this simplified model explains the peculiar shape of the openings with broken parts oriented towards the outside (Figure S3). The proposed model resembles the behavior of a metallic layer (e.g., tungsten) under He<sup>+</sup> ions bombardment<sup>26–28</sup>. In particular, Allen et al.<sup>26</sup> observed swelling and blistering in tungsten single crystals bombarded with He<sup>+</sup> through helium ion microscopy. A blister region was sectioned with FIB and observed at TEM, revealing the presence of a bubble under the layer surface in proximity to the maximum He<sup>+</sup> implantation depth. Similarly, we hypothesize that dimethyl diselenide gas builds up into bubbles within the alumina layer and that such bubbles explode upon reaching a critical overpressure.

## Methods

The spontaneity of the proposed reactions (6, 7, 8, 9) was investigated through the thermodynamic calculation of the Gibbs free energies of reaction ( $\Delta G_r$ ). In particular, the behavior of  $\Delta G_r$  was plotted as a function of pressure and temperature through the polynomial method<sup>29–31</sup> using the data provided by Kubaschewsky et al.<sup>26</sup> (for Se, NaOH, NaF, AlF<sub>3</sub> and Li<sub>2</sub>Se). In case of missing data, Eqs. (2–5) were employed (for CH<sub>3</sub>SeSeCH<sub>3</sub>, Na<sub>2</sub>Se, Al(CH<sub>3</sub>)<sub>3</sub>, Na<sub>2</sub>Se, Na<sub>2</sub>Se<sub>2</sub> and Li<sub>2</sub>Se<sub>2</sub>) starting from tabulated thermochemical data in standard conditions<sup>32–36</sup>.

First, the Gibbs free energy at P<sub>atm</sub> and at the desired temperature (T<sub>2</sub>) ( $\Delta G_f^\circ(T_2, P_{atm})$ ) is calculated through Eq. (2):

$$\Delta G_f^\circ(T_2, P_{atm}) = \Delta H_f^\circ(T_2, P_{atm}) - T_2 \cdot \Delta S_f^\circ(T_2, P_{atm}), \text{ with } T_2 > T; 298 \text{ K} \quad (2)$$

Where  $\Delta H_f^\circ(T_2, P_{atm})$  and  $\Delta S_f^\circ(T_2, P_{atm})$  are the enthalpy and the entropy of formation at T<sub>2</sub> and at P<sub>atm</sub>, respectively. If not reported in the literature  $\Delta H_f^\circ(T_2, P_{atm})$  was calculated with Eq. 3 from the reported value of  $\Delta H_f^\circ$  at room temperature and atmospheric pressure and the heat capacity (C<sub>p</sub>) which was approximated as temperature independent.

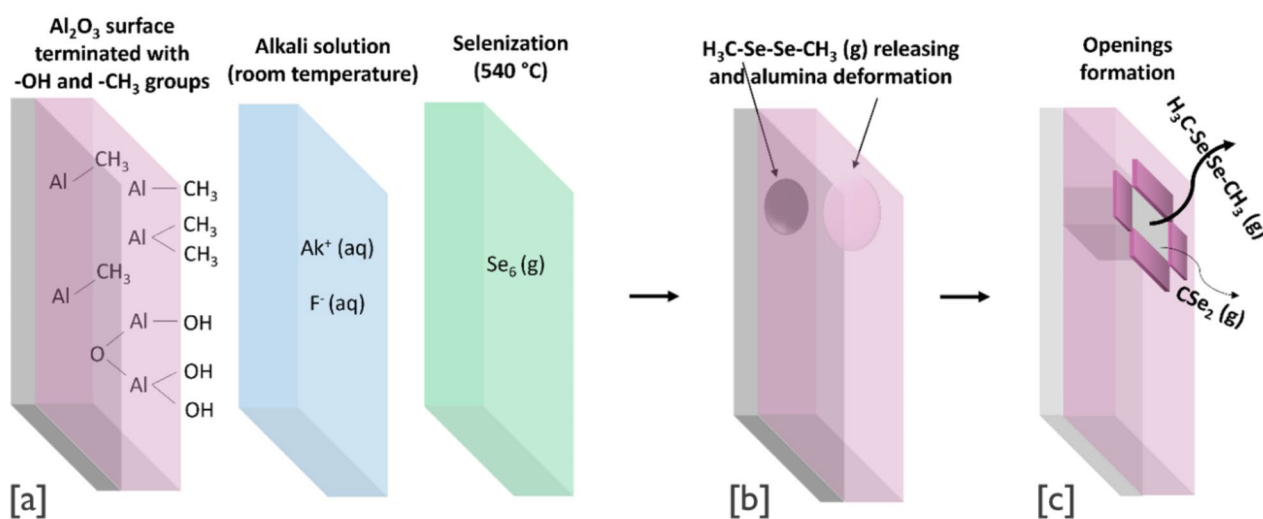


**Fig. 9.** Depiction of the proposed reaction mechanism. (a) Alumina presents -OH and -CH<sub>3</sub> surface termination that, upon the addition of alkali ions and selenium, (b) produces gaseous dimethyl diselenide (and carbon selenide), (c) whose overpressure opens holes in the thin alumina layer.

$$\Delta H_f^\circ(T_2, P_{atm}) = \Delta H_f^\circ(298 K, P_{atm}) \quad (3)$$

Similarly,  $\Delta S_f^\circ(T_2, P_{atm})$ , it can be calculated through Eq. 4 starting from  $\Delta S_f^\circ$  at room temperature and atmospheric pressure that is typically reported in the literature.

$$\Delta S_f^\circ(T_2, P_{atm}) = \Delta S_f^\circ(298 K, P_{atm}) + C_p \cdot \ln(T_2/298) \quad (4)$$

The pressure dependence of  $\Delta G_f^\circ$  was neglected for solids and liquids whereas it was calculated for gas species considering their partial pressures ( $P_x$ ) and the gas moles variation between products and reagents ( $\delta = \text{gas moles in the products} - \text{gas moles in the reagents}$ ) as shown in Eq. 5.

$$\Delta G_f(T_2, P_2) = \Delta G_f^\circ(T_2, P_{atm}) + \delta RT_2 \ln(P_x/P_{atm}) \quad (5)$$

The partial pressure of Se was assumed equal to the overall pressure during the selenization temperature (i.e., ~0.3–0.6 bar), in other words it is considered that only gaseous selenium species are present.

In principle, given the fact that in the experimental conditions of this work dimethyl diselenide is a gas, its partial pressure is missing, hence a wide range of plausible partial pressures were tested to estimate its contribution to the spontaneity of the reactions under study (1,  $10^{-1}$ ,  $10^{-3}$ ,  $10^{-5}$ ,  $10^{-7}$ ,  $10^{-9}$  bar).

For  $\text{CH}_3\text{SeSeCH}_3$  (g) the  $C_p$  and the  $\Delta S_f^\circ$  were not reported for the gas phase, hence the ones for the liquid phase were employed. This is a reasonable approximation as it makes the reaction less favored.

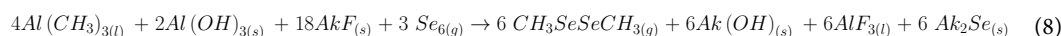
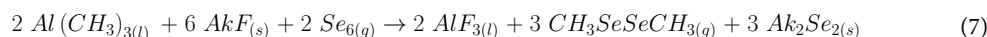
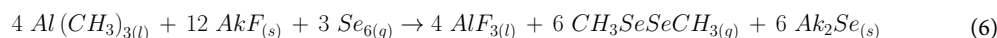
In the proposed model,  $\text{AlF}_3$  is confined to the surface of the alumina layer, where it experiences higher degrees of freedom compared to a solid; hence, its state is considered to be akin to a liquid. In analogy, trimethyl aluminum was considered to be in liquid form and its  $\Delta H_f^\circ$  and  $\Delta S_f^\circ$  were selected accordingly. In case  $C_p$  was not available,  $\Delta H_f^\circ$  was considered temperature independent.  $\text{Na}_2\text{Se}_2$  and  $\text{Li}_2\text{Se}_2$  were considered solid at 540 °C of operation, due to the lack of their melting enthalpy. All the species that come into play were considered anhydrous, which is a reasonable assumption, given the high selenization temperature (~540 °C).

## Model part 2: thermochemical calculations

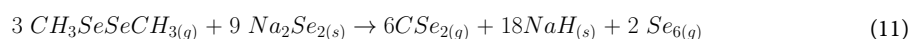
In order to explain the reaction mechanism in more detail, some reactions are proposed, and their thermodynamic spontaneity is investigated (“Methods” for further details). Since the thermodynamic calculations are affected by the stoichiometric coefficients of the species involved, the understanding of which Se molecule is present strongly affects the calculations. Consequently, the Gibbs free energy of formation ( $\Delta G_f$ ) for the different molecular forms of Se are plotted as a function of temperature at the hypothesized Se partial pressures during the selenization process (Fig. 10).  $\text{Se}_6$  appears as the most thermodynamically favored species in a wide temperature range between about 200 °C and 900 °C, including the 540 °C involved during the selenization. The Gibbs free energy behavior as a function of pressure and temperature is calculated through the polynomial method<sup>29–31</sup>, following the data provided by Kubaschewsky et al.<sup>29</sup>, “Methods” for further details regarding the calculations.

Several reactions are plausible, although many of them yield gaseous species such as  $\text{H}_2\text{O}$ ,  $\text{H}_2\text{Se}$ ,  $\text{O}_2$ ,  $\text{SeF}_x$  that are unlikely to be detected via TD-GC-MS measurement due to their very large volatility, and hence were considered unlikely to occur.

As a result, the identified plausible chemical processes entail the direct reaction between alkali (Ak) fluorides, molecular selenium, and trimethyl aluminum with (Eqs. 8, 9) or without (Eqs. 6, 7) the -OH superficial termination onto the alumina layer. The aggregation state of the species involved refers to 540 °C and the reactions that follow are written as they would occur in bulk form.



Both the polynomial method and other calculations were exploited for the estimation of the Gibbs free energy of the reactions (cf. section “Methods”). Reactions in Supplementary Table S1 and S2 are normalized in order to have the same number of  $\text{Al}(\text{CH}_3)_3$  which is believed to be the limiting reagent in order to favor comparison. Unfortunately, due to the unavailability of much thermochemical data, the calculations are complete only for Na and partially for Li, whereas for the remaining alkali ions no calculations are possible. Due to the large number of approximations required (see “Methods”), the end results are only indicative. Despite this, since the difference in  $\Delta G_f$  between reactions in Table S1 and Table S2 is rather large, reactions 5a and 5b are considered more likely to happen, whereas the difference between reaction 6a and 6b is considered to be too small to identify the most spontaneous among the two. TD-GC-MS analyses revealed not only the formation of dimethyl diselenide but also  $\text{CSe}_2$ , whose formation can be justified by considering the reaction of  $\text{CH}_3\text{SeSeCH}_3$  with  $\text{Na}_2\text{Se}$  (Eq. 10) or  $\text{Na}_2\text{Se}_2$  (Eq. 11) or considering the reaction of  $\text{Na}_2\text{Se}_2$  with  $\text{Al}(\text{CH}_3)_3$  and NaF (Eq. 12).



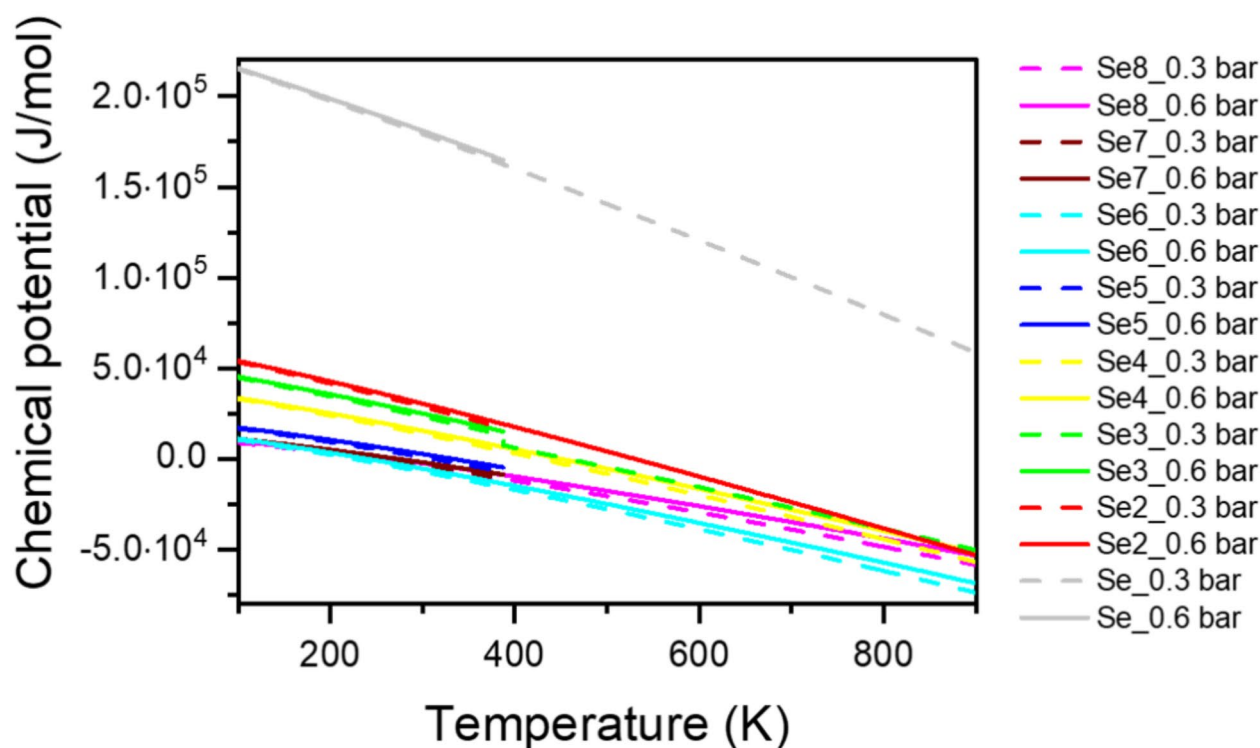


**Fig. 10.** Thermodynamic stability of possible Se molecular species formed. The Gibbs free energy of different Se molecular species is plotted as a function of temperature at two different pressures. Data supporting Fig. 10 is available as supporting excel file named “Thermochemistry Se”.

### Summary and outlook

This study provides a comprehensive investigation into the creation of nano- and micron-sized openings in dielectric layers through the selenization of as-prepared aluminum oxide layers in the presence of alkali metals. The required temperature and duration of the selenization are different for each halide alkali metal salt, which can be explained by the difference in their lattice constants and dissociation enthalpies. The mechanism and chemistry of the process are explained as follows: holes form spontaneously in alumina layers if Se and alkali salts are present along with residual unreacted methyl groups. Comprehensive reactions are written to explain the chemical processes behind the formation of openings. These equations entail the direct reaction of trimethyl aluminum with alkali fluorides and selenium with or without -OH groups onto the alumina surface. The thermochemistry of the aforementioned reactions was investigated showing the spontaneity of those reactions in most of the thermodynamic conditions tested. Our thermochemical assessment is conservative (our conclusions sound) since an excess of selenium can lead to a number of alkali-polyselenides with higher stability in lieu of the  $\text{Ak}_2\text{Se}$  species. This study paves the way to a deeper understanding of the hole formation onto alumina layer during a selenization process in the presence of alkali salts. Also, as an example application area, solar cells' rear and front surfaces can be passivated with the chosen alkali metal halide in an industrially viable way by using this approach. The type of the dielectric layer can also be altered if the source of the layer consists of methyl-based gases. By changing the alkali metal halide salt deposition technique with a more controllable approach, like slot-dye coating, or spray pyrolysis, the size and distribution of the created openings can also be controlled and hence, well-defined openings in the dielectric layer are obtained. Furthermore, dielectric layers have various usage areas, and being able to make alterations in the layers at low temperatures can be another advantage of the proposed study.

### Data availability

The datasets generated and/or analyzed during the current study are not publicly available due to the requirement of confidentiality but are available from the corresponding author on reasonable request.

Received: 12 December 2023; Accepted: 5 November 2024

Published online: 09 November 2024

### References

1. Wang, S. et al. Mechanically and thermally stable, transparent electrodes with silver nanowires encapsulated by Atomic Layer Deposited Aluminum Oxide for Organic Optoelectronic devices. *Org. Electron.* **78** (October 2019), 105593. <https://doi.org/10.1016/j.orgel.2019.105593> (2020).

2. Gupta, V., Bhatt, V. & Chandra, S. R. F. Magnetron Sputtered Aluminum Oxide Films for MEMS. Proc. 14th Int. Work. Phys. Semicond. Devices, IWPSD 682–685. (2007). <https://doi.org/10.1109/TWPSD.2007.4472611>
3. Daus, A. et al. Aluminum Oxide as a Dielectric and Passivation Layer for (Flexible) Metal-Oxide and 2D Semiconductor Devices. In Proc.SPIE;11687. (2021). <https://doi.org/10.1117/12.2587997>
4. Bonilla, R. S., Hoex, B., Hamer, P. & Wilshaw, P. R. Dielectric Surface Passivation for Silicon Solar Cells: a review. *Phys. Status Solidi*. **214** (7), 1700293. <https://doi.org/10.1002/pssa.201700293> (2017).
5. Liu, F. et al. Beyond 8% ultrathin kesterite Cu<sub>2</sub>ZnSnS<sub>4</sub> solar cells by interface reaction Route Controlling and Self-Organized Nanopattern at the Back Contact. *NPG Asia Mater.* **9** (7), e401–e401. <https://doi.org/10.1038/am.2017.103> (2017).
6. Gopikrishnan, C. R., Jose, D., Datta, A. E. & Structure Lattice Energies and born exponents for Alkali Halides from First principles. *AIP Adv.* **2** (1), 012131. <https://doi.org/10.1063/1.3684608> (2012).
7. Birant, G., Wild, J., De; Meuris, M., Poortmans, J. & Vermang, B. Dielectric-based rear surface passivation approaches for Cu (in, Ga) Se<sub>2</sub> solar cells — a review. *Appl. Sci.* **9** (677). <https://doi.org/10.3390/app9040677> (2019).
8. Johnson, R. W., Hultqvist, A. & Bent, S. F. A brief review of atomic layer deposition: from fundamentals to applications. *Mater. Today*. **17** (5), 236–246. <https://doi.org/10.1016/j.mattod.2014.04.026> (2014).
9. Birant, G. et al. Innovative and industrially viable Approach to Fabricate AlO<sub>x</sub> Rear Passivated Ultra-thin Cu(in, Ga)Se<sub>2</sub> (CIGS) Solar cells. *Sol Energy* (2020).
10. Ledinek, D., Keller, J., Hägglund, C., Chen, W. C. & Edoff, M. Effect of NaF Pre-Cursor on Alumina and Hafnia Rear Contact Passivation Layers in Ultra-Thin Cu(In,Ga)Se<sub>2</sub> Solar Cells. *Thin Solid Films* 683 (November 2018), 156–164. <https://doi.org/10.1016/j.tsf.2019.05.024> (2019).
11. Kotipalli, R. R. *Surface Passivation Effects of Aluminum Oxide on Ultra-Thin CIGS Solar Cells* (Université Catholique de Louvain, 2016).
12. Salomé, P. M. P. et al. Passivation of interfaces in Thin Film Solar cells: understanding the effects of a Nanostructured Rear Point Contact Layer. *Adv. Mater. Interfaces*. **5**(2), 1701101. <https://doi.org/10.1002/admi.201701101> (2018).
13. Casper, P. et al. Optoelectrical improvement of Ultra-thin Cu(in,Ga)Se<sub>2</sub> solar cells through Microstructured MgF<sub>2</sub> and Al<sub>2</sub>O<sub>3</sub> Back Contact Passivation Layer. *Phys. Status Solidi - Rapid Res. Lett.* **10** (5), 376–380. <https://doi.org/10.1002/pssr.201600018> (2016).
14. Ledinek, D., Donzel-gargand, O., Sköld, M., Keller, J. & Edo, M. Effect of different na supply methods on thin cu(in,Ga)Se<sub>2</sub> solar cells with Al<sub>2</sub>O<sub>3</sub> rear passivation layers. *Sol Energy Mater. Sol Cells*. **187** (July), 160–169. <https://doi.org/10.1016/j.solmat.2018.07.017> (2018).
15. Birant, G. et al. Rear surface passivation of Ultra-thin CIGS Solar cells using atomic layer deposited HfO<sub>x</sub>. *EPJ Photovoltaics*. **11**, 10. <https://doi.org/10.1051/epjpv/2020007> (2020).
16. de Wild, J. et al. Detrimental impact of na upon rb postdeposition treatments of Cu(in,Ga)Se<sub>2</sub> Absorber Layers. *Solar RRL*. **5** (9), 2100390. <https://doi.org/10.1002/solr.202100390> (2021).
17. Kandybka, I. et al. Novel cost-effective Approach to produce Nano-Sized Contact openings in an aluminum oxide passivation layer up to 30 nm Thick for CIGS Solar cells. *J. Phys. D Appl. Phys.* **54** (23), 234004. <https://doi.org/10.1088/1361-6463/abed09> (2021).
18. Vermang, B. et al. On the blistering of atomic layer deposited Al<sub>2</sub>O<sub>3</sub> as Si surface passivation. In *2011 37th IEEE Photovoltaic Specialists Conference*. 003562–003567 (Seattle, WA, USA, 2011). <https://doi.org/10.1109/PVSC.2011.6185916>.
19. Ostermna, V. & Antes, H. Critical Melting Points and Reference Data for Vacuum Heat Treating. *Sol Vac Furn Ref. Ser.* **1**, 42. (2010).
20. Hammett, L. P. The Effect of structure upon the reactions of Organic compounds. *Benzene Derivatives J. Am. Chem. Soc.* **59**, 96–103 (1937).
21. Sverjensky, D. & Molling, P. A linear free energy relationship for crystalline solids and aqueous ions. *Nature*. **356**, 231–234 (1992).
22. Investigation of Chalcogenide Absorber Materials for Photovoltaic Applications, Colombara, D. & Author Jul). **31** (2012).
23. Bielinski, A. R., Kamphaus, E. P., Cheng, L. & Martinson, A. B. F. resolving the Heat of Trimethylaluminum and Water Atomic layer deposition half-reactions. *J. Am. Chem. Soc.* **144**, 15203–15210 (2022).
24. Dillion, A. C., Ott, A. W., Way, J. D. & George, S. M. Surface chemistry of Al, o, deposition using Al(CH<sub>3</sub>)<sub>3</sub> and H<sub>2</sub>O in a binary reaction sequence. *Surf. Sci.* **322**, 230–242 (1995).
25. Goldstein, D. N., McCormick, J. A. & George, S. M. Al<sub>2</sub>O<sub>3</sub> Atomic Layer deposition with trimethylaluminum and ozone studied by in situ transmission FTIR Spectroscopy and Quadrupole Mass Spectrometry. *J. Phys. Chem. C*. **112**, 19530–19539 (2008).
26. Allen, F. I., Hosemann, P. & Balooch, M. Key mechanistic features of swelling and blistering of Helium-ion-irradiated tungsten. *Scr. Mater.* **178**, 256–260 (2020).
27. Evans, J. H. The role of implanted gas and lateral stress in blister formation mechanisms. *J. Nucl. Mater.* **76–77**, 228–234 (1978).
28. EerNisse, E. P. & Picraux, S. T. Role of integrated lateral stress in surface deformation of He- implanted surfaces. *Ournal Appl. Phys.* **48**, (1977).
29. Knacke, O., Kubaschewsky, O. & Hesselmann, K. Thermochemical properties of inorganic substances. (1991).
30. McBride, J., Gordon, S. & Reno, A. Coefficients thermodynamic properties for calculating and Transport species of Individual. *NASA Tech. Memo* 4513, 4–5 (1993).
31. Burcat, A., Zeleznik, F. J. & McBride, B. J. Ideal Gas Thermodynamic Properties for the Phenyl, Phenoxy and o-Biphenyl Radicals. *NASA Tech. Memo* 83800 NASA-TM-83. <https://ntrs.nasa.gov/citations/19850013894> (1985).
32. Olin, Å., Nolang, B., Osadchii, G., Öhman, E. & Rosen, E. L.-O. CHEMICAL THERMODYNAMICS OF SELENIUM, vol. 7. Nuclear Energy Agency, Data Bank Issy-les-Moulineaux (France).
33. Wagman, D. D. et al. The NBS tables of chemical thermodynamic properties selected values for inorganic C1 and C2 organic substances in SI units. *Phys. Chem. Ref. Data* **11**, (1982).
34. McCullough, B. J. P., Messerly, J. F., Moore, R. T. & Todd, S. S. Thermodynamic functions in the solid and trimethylaluminum: liquid states, 0–380 ° k; vapor pressure, heat of vaporization, and entropy in the ideal gas state. *Thermodyn. Prop. Trimethylaluminum*. **67**(3), 677–679. <https://doi.org/10.1021/j100797a033> (1963).
35. Webbook, N. I. S. T. & WebBook S. 69. <https://webbook.nist.gov/cgi/cbook.cgi?Source=1963MOR%2FSEL0&Mask=2#ref-8>
36. BIDAÏ, K. et al. FP-LAPW investigation of mechanical and thermodynamic properties of Na<sub>2</sub>X (X=S and Se) under pressure and temperature effects. *Mater. Sci.* **33**, 649–659 (2015).

## Author contributions

Conceptualization: Gizem Birant (G.B) (equal), Jessica de Wild (J.dW.) (equal), Bart Vermang (B.V.) (equal)  
 Investigation: G.B. (lead) Methodology: G. B. (lead), J.dW. (equal), Wouter Marchal (W.M.) (supporting),  
 Christian Rossi (C.R.) (supporting), Diego Colombara (D.C.) (supporting), Jan Czech (J.C.) (supporting)Data  
 curation: G.B. (lead), C.R. (equal)Formal analysis: G.B. (lead), J.dW. (equal), C.R. (supporting), D.C. (sup-  
 porting), W.M. (supporting)Project administration: G.B. (equal), J.dW. (equal), B.V. (equal)Supervision: J.dW.  
 (equal), B.V. (equal)Writing – original draft: G.B. (lead) Writing – review & editing: G.B. (lead), J.dW.  
 (equal), B.V. (supporting), W.M. (supporting), C.R. (equal), D.C. (equal), J.C. (supporting), Guy Brammertz  
 (G.Br.) (supporting), Tom Aernouts (T.A.) (supporting)Funding acquisition: B.V. (lead), J.dW. (equal), G.B.  
 (equal)Project administration: B.V. (lead), J.dW. (equal), G.B. (equal) Resources: B.V. (lead), T.A. (equal)Vali-

ation: J.dW. (equal), B.V. (equal), D.C. (equal) Visualization: G.B. (lead), C.R. (equal) All authors reviewed the manuscript.

### Funding

This work received funding from the European Union's H2020 research and innovation program under grant agreement No. 715027 (Uniting PV). Authors thank Research Foundation - Flanders (FWO) for the funding through the project number 1219423 N (ARLEA) and G0A1623N (ENGAGED).

### Declarations

### Competing interests

The authors declare no competing interests.

### Additional information

**Supplementary Information** The online version contains supplementary material available at <https://doi.org/10.1038/s41598-024-78919-w>.

**Correspondence** and requests for materials should be addressed to G.B.

**Reprints and permissions information** is available at [www.nature.com/reprints](http://www.nature.com/reprints).

**Publisher's note** Springer Nature remains neutral with regard to jurisdictional claims in published maps and institutional affiliations.

**Open Access** This article is licensed under a Creative Commons Attribution-NonCommercial-NoDerivatives 4.0 International License, which permits any non-commercial use, sharing, distribution and reproduction in any medium or format, as long as you give appropriate credit to the original author(s) and the source, provide a link to the Creative Commons licence, and indicate if you modified the licensed material. You do not have permission under this licence to share adapted material derived from this article or parts of it. The images or other third party material in this article are included in the article's Creative Commons licence, unless indicated otherwise in a credit line to the material. If material is not included in the article's Creative Commons licence and your intended use is not permitted by statutory regulation or exceeds the permitted use, you will need to obtain permission directly from the copyright holder. To view a copy of this licence, visit <http://creativecommons.org/licenses/by-nc-nd/4.0/>.

© The Author(s) 2024